OPAL Physics Note PN 276
21. February 1997

Multi-Photon Final States in e^+e^- Collisions at $\sqrt{s} = 161$ and 172 GeV

The OPAL Collaboration

Abstract

The process $e^+e^- \rightarrow \gamma\gamma(\gamma)$ is studied with the OPAL detector at LEP. The data sample corresponds to integrated luminosities of 10.3 and 10.4 pb^{-1} taken at centre-of-mass energies of 161 and 172 GeV, respectively. The measured cross-section agrees well with the expectation from QED. In a combined fit using data from both centre-of-mass energies, the angular distribution is used to set improved limits on the cut-off parameters: $\Lambda_+ >$ 194 GeV and $\Lambda_- >$ 211 GeV (95% CL). These are the highest limits obtained to date compared to previous LEP results and other experiments at lower energies. Limits on non-standard $e^+e^-\gamma$ couplings and contact interactions, as well as a mass limit for an excited electron $M_{e^*} > 192$ GeV with $\kappa = 1$, are determined.

This note describes preliminary OPAL results to be submitted to the XVIII International Symposium on Lepton-Photon Interactions, Hamburg, 28 July - 1 August 1997

1 Introduction

This analysis studies the annihilation process $e^+e^- \to \gamma\gamma(\gamma)$ with the OPAL detector at LEP. At LEP energies, this is one of the few processes having negligible contributions from the weak interaction. Since the QED differential cross-section is extremely well known, measurement of this angular distribution provides complementary tests of non-standard physics processes which can contribute to these photonic final states.

The OPAL collaboration has previously published a search for photonic final states with and without missing energy at $\sqrt{s} = 130 - 140$ GeV [1]. The present analysis concentrates on final states with two and more detected photons, with no missing transverse momentum, to study the QED process only. Photonic final states with missing energy have been analyzed separately searching for new particle production [2].

It is possible to improve the present precision for measuring deviations from QED by using the data taken at centre-of-mass energies of 161 GeV and 172 GeV. The corresponding integrated luminosities of these data sets are 10.3 and 10.4 pb^{-1} respectively. Non-QED effects, should they exist, are expected to increase with centre-of-mass energy. For the analysis of the process $e^+e^- \to \gamma\gamma(\gamma)$, the centre-of-mass energy range around the Z^0-peak has no advantage over other energy ranges for most physics models. The cross-section is hardly influenced by the weak interaction, whereas background processes that can be mediated by a Z^0 are increased by roughly two orders of magnitude. The ratio of the cross-section for background (e.g. Bhabha events) to photon production becomes much smaller off the Z^0-peak. Thus systematic errors due to background decrease at higher energies.

The possible effects of an excited electron, e^*, are also investigated. An excited electron with $e^*e\gamma$ coupling will contribute to the process $e^+e^- \to \gamma\gamma(\gamma)$ via t-channel exchange. A comparison of the measured angular distribution with the QED prediction yields limits on the e^* mass.

The three photon final state production process $e^+e^- \to \gamma\gamma\gamma$ could have contributions from $e^+e^- \to Z^0 \to \gamma\gamma\gamma$ with a non-standard $Z^0\gamma\gamma\gamma$ four boson coupling [3]. The statistical significance of this contribution, based on an integrated luminosity of 100 pb^{-1}, is however decreased by roughly a factor four compared to the energy range around the Z^0-peak.

At energies studied in this analysis one can investigate the production of a resonance X via $e^+e^- \to X\gamma$ followed by the decay $X \to \gamma\gamma$. This process would lead to a three photon final state without missing energy. The resonance should show up in the spectrum of the invariant mass of a photon pair. The special case of a scalar resonance or the Higgs is discussed in Ref. [4].

A detailed description of the OPAL detector can be found in [5]. For this analysis the most important detector component is the electromagnetic calorimeter (ECAL) consisting of 13968 lead-glass blocks covering 98% of the solid angle. The central tracking detector is used primarily to reject events inconsistent with photonic final state topologies. The analysis uses raw data to provide hit information in the vertex drift chamber (CV) and jet drift chamber (CJ). CV is divided into 36 sectors and covers 95% of the solid angle with its 12 axial layers. The coverage is increased to 97% if only the inner 6 axial layers are used. CJ is divided into 24 sectors and covers 97% of the solid angle with its inner 16 layers.

In section 2, the differential cross-sections for the QED process as well as for several models having deviations from QED are provided. In section 3 – 5 the analysis is described in detail. The results are presented in section 6.

2 Cross section for the process $e^+e^- \rightarrow \gamma\gamma$

The differential cross-section for the process $e^+e^- \rightarrow \gamma\gamma$ in lowest order QED is given by [6]:

$$\left(\frac{d\sigma}{d\Omega}\right)_{\text{Born}} = \frac{\alpha^2}{s\beta}\left[\frac{1+\beta^2(1+\sin^2\theta)}{1-\beta^2\cos^2\theta} - \frac{2\beta^4\sin^4\theta}{(1-\beta^2\cos^2\theta)^2}\right] \tag{1}$$

where s denotes the square of the centre-of-mass energy, β is the beam velocity and θ the polar angle of one photon. Since the two photons cannot be distinguished the event angle is defined such that $\cos\theta$ is positive. At high centre-of-mass energies the relativistic limit $\beta \approx 1$ is valid and equation (1) simplifies to

$$\left(\frac{d\sigma}{d\Omega}\right)_{\text{Born}} = \frac{\alpha^2}{s}\,\frac{1+\cos^2\theta}{1-\cos^2\theta}. \tag{2}$$

In Reference [7] deviations from the QED cross-section for Bhabha and Møller scattering are parametrized in terms of cut-off parameters. These parameters correspond to a short range exponential term added to the Coulomb potential. This ansatz leads to a modification of the photon angular distribution as given in eq. (3). Several models with a gauge invariant effective Lagrangian adding contact interactions ($\gamma\gamma e^+e^-$) or non-standard γe^+e^- couplings to the QED interaction are described in Ref. [8]. These lead to angular distributions with different mass scales Λ (see eqs. 4 - 6). The subscripts (QED+6 etc.) follow the notation in Ref. [8].

$$\left(\frac{d\sigma}{d\Omega}\right)_{\Lambda_\pm} = \left(\frac{d\sigma}{d\Omega}\right)_{\text{Born}}\left[1 \pm \frac{s^2}{2\Lambda_\pm^4}\sin^2\theta\right] \tag{3}$$

$$\left(\frac{d\sigma}{d\Omega}\right)_{\text{QED+6}} = \left(\frac{d\sigma}{d\Omega}\right)_{\text{Born}}\left[1 + \frac{s^2}{\alpha\Lambda^4}\sin^2\theta\right] \tag{4}$$

$$\left(\frac{d\sigma}{d\Omega}\right)_{\text{QED+7}} = \left(\frac{d\sigma}{d\Omega}\right)_{\text{Born}} + \frac{s^2}{32\pi}\frac{1}{\Lambda^6} \tag{5}$$

$$\left(\frac{d\sigma}{d\Omega}\right)_{\text{QED+8}} = \left(\frac{d\sigma}{d\Omega}\right)_{\text{Born}} + \frac{s^2 m_e^2}{32\pi}\frac{1}{\Lambda^8} \tag{6}$$

The definition of equation (4) is essentially identical to the standard definition (eq. 3). Equations (5) and (6) also describe equivalent deviations from the angular distribution predicted by QED. Therefore only the parameters of equations (3) and (5) are determined.

The existence of an excited electron e^* with $e^*e\gamma$ coupling would contribute to the photon production process via t-channel exchange. The resulting deviation from $\left(\frac{d\sigma}{d\Omega}\right)_{\text{Born}}$ depends on the mass M_{e^*} and the coupling constant κ of the $e^*e\gamma$ vertex [9].

$$\begin{aligned}
\left.\frac{d\sigma}{d\Omega}\right|_{e^*} &= \left(\frac{d\sigma}{d\Omega}\right)_{\text{Born}} + \\
\alpha^2 \Bigg\{ & \frac{1}{2}\left(\frac{\kappa}{M_{e^*}}\right)^4 \left(E^2\sin^2\theta + M_{e^*}^2\right)\left(\frac{q^4}{(q^2-M_{e^*}^2)^2} + \frac{q'^4}{(q'^2-M_{e^*}^2)^2}\right) \\
&+ 4\left(\frac{\kappa}{M_{e^*}}\right)^4 \frac{M_{e^*}^2\, E^4\, \sin^2\theta}{(q^2-M_{e^*}^2)(q'^2-M_{e^*}^2)} \\
&+ \left(\frac{\kappa}{M_{e^*}}\right)^2 \left[\frac{q^2}{q^2-M_{e^*}^2} + \frac{q'^2}{q'^2-M_{e^*}^2} + E^2\sin^2\theta\left(\frac{1}{q^2-M_{e^*}^2} + \frac{1}{q'^2-M_{e^*}^2}\right)\right]\Bigg\}
\end{aligned} \tag{7}$$

with the beam energy $E = \sqrt{s}/2$, $q^2 = -2E^2(1-\cos\theta)$ and $q'^2 = -2E^2(1+\cos\theta)$.

3 Event angle definition

For the process $e^+e^- \to \gamma_1\gamma_2$ the polar angle θ of the event is defined by the angle between either of the two photons and the beam direction since $|\cos\theta_1| = |\cos\theta_2|$. At $\mathcal{O}(\alpha^3)$ the multi-differential cross-section $\frac{d^5\sigma}{d\Omega}$ of events with three photons is a function of 5 variables, for example the polar and azimuthal angles of the two most energetic photons θ_1, ϕ_1, θ_2, ϕ_2 and the energy of the third photon E_3. Thus in general $|\cos\theta_1| \neq |\cos\theta_2|$ if there is a third photon. Several definitions are possible to characterize an event. The following two are studied:

$$\cos\theta_{\mathrm{av}} = \frac{|\cos\theta_1| + |\cos\theta_2|}{2} \quad (8)$$

$$\cos\theta^* = \left|\sin\frac{\theta_1-\theta_2}{2}\right| \Big/ \sin\frac{\theta_1+\theta_2}{2} \quad (9)$$

The angle $\cos\theta_{\mathrm{av}}$ is just the average of the two photon angles. The angle $\cos\theta^*$ is identical to $|\cos\theta|$ for two-photon final states. For three-photon events in which the third photon is along the beam direction it is equivalent to the scattering angle in the centre-of-mass system of the two observed photons. To minimize higher order effects, the $\cos\theta$ distribution for the chosen definition of θ should have the same shape as the distribution from the lowest order calculation. The total cross-section may differ which would result in a normalization factor ϵ.

The angular distribution according to both definitions of $\cos\theta$ are shown in Figure 1 using a $\mathcal{O}(\alpha^3)$ Monte Carlo generator [10]. The event angles are calculated from the two photons with the highest generated energy. The comparison is done at the generator level, i.e. without detector simulation and efficiency effects. It can be seen that the distribution of $\cos\theta_{\mathrm{av}}$ (eq. 8) shows large deviations from the lowest order (Born) distribution for much of the $\cos\theta$ range. In this analysis the definition according to equation (9) is chosen because it matches well the Born distribution for most of the range. The distribution shows an increased total cross-section and has large deviations from the Born distribution for $\cos\theta^* > 0.95$. This is not a problem, since events with $\cos\theta^* > 0.9$ are not considered in this analysis, because the efficiency decreases for these angles (see sect. 5). The angular deviation within the used $\cos\theta^*$ range is smaller than 5% and will be corrected.

4 Event selection

Events are selected by requiring two or more clusters in the electromagnetic calorimeter (ECAL). These clusters are selected as photon candidates if they are within the polar angle range of $|\cos\theta| < 0.97$. The energy deposit E_{raw} in the ECAL must exceed 1 GeV and the cluster must consist of at least 2 lead-glass blocks.

There are two major groups of background sources. The first consists of processes with primary charged tracks. Especially Bhabha events, with similar event characteristics, cannot be distinguished otherwise. The other group are events without primary charged tracks. Cosmic events and the process $e^+e^- \to \bar{\nu}\nu\gamma\gamma$ contribute to this background.

4.1 Neutral events

Events having only final state photons are classified as 'neutral events'. They should not have any charged track coming from the interaction point. However, to reject all events having tracks in CV or CJ would lead to an efficiency loss because of converted photons. The efficiency for selecting converted photons should be as high as possible in order to make the analysis less sensitive to the conversion probability and therefore to the detector simulation. On the other hand, contributions from any channel with primary charged tracks should be reduced to a negligible level. In particular, Bhabha events can fake photons if one or both tracks are not reconstructed. Electrons from Bhabha events as well as photons from the QED process deposit nearly all their energy in the ECAL and produce highly energetic clusters. Furthermore the event characteristics (two collinear particles) are very similar.

To reject events with primary charged tracks the following vetos are defined. First the correlation between charged track activity in both drift chambers and the observed clusters is investigated. Hits are counted in the ϕ-sectors of CV and CJ which are geometrically associated to each cluster. A correlation is assigned to a cluster if there are more than a given number of wires with hits in the ϕ-sector of the cluster.

- In CV the number of required wires with hits depends on the $\cos\theta$ of the cluster. A CV correlation is assigned if there are at least m wires with hits in the n CV layers nearest to the beam-pipe (denoted by m/n). Only one hit per layer is counted.

Cut on m/n	$\cos\theta$ region
6/12	$0. < \lvert\cos\theta\rvert < 0.75$
5/8	$0.75 < \lvert\cos\theta\rvert < 0.95$
4/6 or 5/8	$0.95 < \lvert\cos\theta\rvert < 1.$

- A CJ correlation is assigned if there are at least 12 wires with hits in the inner 16 CJ layers independent of the cluster angle.

Two vetos are defined as combinations of charged track activity correlations in CV and CJ. A third veto tests for charged tracks not correlated with any of the clusters. Any of the three vetos rejects the event.

- The **single veto** corresponds to clear charged particle activity along with one cluster. If both the CV and CJ correlation are assigned to the same cluster the event is vetoed.
- The **double veto** corresponds to some charged particle activity along with both clusters, e.g. two badly reconstructed tracks. If either the CV or CJ correlation is assigned to both clusters, the event is vetoed.
- The **track veto** demands that there be no reconstructed charged track outside 15° in ϕ of all photon candidates. The track must have a transverse momentum of more than 1 GeV, at least 20 hits in CJ and at least 4 axial wire hits in CV.

4.2 Kinematic selection

The event sample is divided into three classes *I*, *II* and *III*. They are distinguished by the number of photon candidates and the acollinearity ζ defined as $\zeta = 180^\circ - \xi$, where ξ is the three-dimensional angle between the two highest energy clusters. Cuts are defined for each class separately to reduce background. A cut on $\cos\theta^* < 0.9$ is applied for all events to avoid systematic errors due to large corrections since the efficiency decreases strongly for small event angles as will be shown in the next section.

All events having the two highest energy clusters collinear belong to class *I* independent of the number of photon candidates. The acollinearity requirement is $\zeta < 10^\circ$. For true $e^+e^- \to \gamma\gamma(\gamma)$ events, the sum of the two highest cluster energies $\sum E$ should yield the centre-of-mass energy $\sqrt{s}$. The distribution of $\sum E$ is shown in Figure 2. A cut is applied at $\sum E > 0.6\sqrt{s}$. This is well below the tail of the energy distribution which is represented by the Monte Carlo. 86% of the selected data events are of this type.

The class *II* contains events having the two highest energy clusters acollinear ($\zeta > 10^\circ$) and exactly two observed photon candidates. Usually this class contains events with one photon escaping detection by going down the beam-pipe ($|\cos\theta| > 0.97$). If the polar angle of this photon is assumed to satisfy $|\cos\theta| = 1$, its energy E_{gone} can be calculated from the angles of the observed photons θ_1 and θ_2. The energy sum $\sum E$ is then defined as the sum of both observed cluster energies and the lost energy.

$$\begin{aligned} E_{\mathrm{gone}} &= \eta\sqrt{s} \\ \eta^{-1} &= 1 + \frac{\sin\theta_1 + \sin\theta_2}{|\sin(\theta_1 + \theta_2)|} \\ \sum E &= E_1 + E_2 + E_{\mathrm{gone}} \end{aligned} \tag{10}$$

The variable $\Delta\phi$, defined as

$$\Delta\phi = (\sin\theta_1 + \sin\theta_2)\cos^2\left(\frac{\phi_1 - \phi_2}{2}\right) \tag{11}$$

provides an approximate measure of the scaled transverse momentum of the event which does not use the cluster energies. Figure 3 shows the distributions of $\Delta\phi$ and $\sum E$. A cut is applied at $\Delta\phi < 0.1$ and $\sum E > 0.6\sqrt{s}$. The angular definition discussed in section 3 uses the two highest energy photons. It is not possible to calculate the correct event angle if one of these has escaped the detector. If one of the two hardest photons has escaped detection then the incorrectly determined event angle would lead to a depopulation of events at $\cos\theta^*$ near 1 with a consequent increase in events at lower $\cos\theta^*$. In the barrel region, where the cross-section is small, the relative deviation would be up to 20%. Therefore events are rejected if E_{gone} exceeds either E_1 or E_2.

The class *III* contains events having the two highest energy clusters acollinear ($\zeta > 10^\circ$) and n photon candidates ($3 \le n \le 5$) with cluster energies E_i. The number of events expected from QED photon production with more than five photons is negligible. Instrumental background however can produce events with many clusters. Therefore in this note we restrict the maximum number of photon candidates to five. Transverse and longitudinal momentum (p_{t}, p_{l}) of the system are calculated. Since a non-zero longitudinal momentum could correspond to an additional photon along the beam direction, the energy sum $\sum E$ is calculated as sum of the cluster energies and p_{l}.

$$\sum E = \sum_{i=1}^{n} E_i + p_{\mathrm{l}} \tag{12}$$

The angle sum $\sum \alpha$ is used to identify three photon events, which should be planar:

$$\sum \alpha = \alpha_{ij} + \alpha_{ik} + \alpha_{kj}, \tag{13}$$

with α_{ij} the angle between photons i and j. Figure 4 shows the distribution of p_{t} versus $\sum E$ for $\mathrm{e^+e^-} \rightarrow \gamma\gamma(\gamma)$ Monte Carlo and for the data. In the data the $\mathrm{e^+e^-} \rightarrow \gamma\gamma(\gamma)$ events are clearly separated from the background by the fact that they have small transverse momenta and an energy sum about the centre-of-mass energy. The background are cosmic events and instrumental background mainly. The applied cuts are indicated and given in Table 1. No event with more than three clusters is observed. In Table 2 the characteristics of the selected events are listed. Five planar events with $\sum \alpha > 355°$ are accepted as three photon events and included in the sample of $\mathrm{e^+e^-} \rightarrow \gamma\gamma(\gamma)$. Two other events are consistent with three detected photons and an additional photon along the beam direction.

For all three classes 102 (94) events were selected at $\sqrt{s} = 161$ (172) GeV. They were scanned visually to check for background. All events were found to be consistent with the topology of the process $\mathrm{e^+e^-} \rightarrow \gamma\gamma(\gamma)$. None were rejected on the basis of the scan. The kinematic cuts used for each of the event classes are summarized in Table 1.

The invariant mass of each photon pair is shown in Figure 5 for all events with three photons, e.g. classes *II* and *III*. There are three entries for events with three clusters. A resonance X produced in the process $\mathrm{e^+e^-} \rightarrow \mathrm{X}\gamma$ and decaying photonically $\mathrm{X} \rightarrow \gamma\gamma$ would contribute to these events. The mass resolution for photonic events is 3 GeV. The distribution agrees well with the Monte Carlo expectation from the process $\mathrm{e^+e^-} \rightarrow \gamma\gamma(\gamma)$. No enhancement due to a resonance is observed.

Event class	Cuts
I	$\zeta < 10°$ $\sum E > 0.6\sqrt{s}$
II	$\zeta > 10°$ $\sum E > 0.6\sqrt{s}$ $E_1, E_2 > E_{\mathrm{gone}}$ $\Delta\phi < 0.1$ 2 photon candidates
III	$\zeta > 10°$ $\sum E - 5p_t > 0.5\sqrt{s}$ $\sum E < 1.3\sqrt{s}$ $p_t < 0.09\sqrt{s}$ 3 – 5 photon candidates
all	$\cos\theta^* < 0.9$

Table 1: Summary of the kinematic cuts. For definition of the variables see the text.

$\sqrt{s}$ [GeV]	n	$\cos\theta^*$	$\sum E/\sqrt{s}$	$p_t/\sqrt{s}$	$p_l/\sqrt{s}$	$\sum\alpha$ [deg]
161	3	0.345	0.993	0.003	0.031	359.9
161	3	0.637	0.933	0.051	0.046	360.0
161	3	0.273	0.975	0.059	0.113	358.1
161	3	0.865	0.982	0.036	0.334	326.1
172	3	0.697	1.008	0.018	0.019	360.0
172	3	0.413	0.984	0.012	0.108	359.4
172	3	0.668	0.874	0.015	0.372	313.8

Table 2: Event characteristics for the *III* class. The centre-of-mass energy, number of photon candidates, event angle, scaled energy sum, scaled transversal and longitudinal momentum as well as the angle sum are given.

5 Systematic errors

The effect of radiative corrections is quantified by $\mathcal{R}$, the ratio of the Monte Carlo angular distribution and the Born cross-section as shown in Figure 1.

$$\mathcal{R} = \left(\frac{d\sigma}{d\Omega}\right)_{\mathrm{MC}} (\cos\theta^*) \Bigg/ \left(\frac{d\sigma}{d\Omega}\right)_{\mathrm{Born}} \tag{14}$$

The ratio $\mathcal{R}$ is used to correct the data bin by bin to Born level. No error on the angular dependence is included in the correction; only a 1% error on the total cross-section is taken into account. Omitting the angular dependence and correcting only the increased total cross-section would change the central value for the later results for cut-off parameters and mass scales by 10% of the 1σ error. But the lower limits would change by 1% only. The problem is very non-linear and the physical result is the limit but not the central value. Since the $\mathcal{O}(\alpha^3)$ radiative corrections are small the $\mathcal{O}(\alpha^4)$ effects are assumed to be negligible. No Monte Carlo with a complete 4th order calculation is currently available.

The efficiency and angular resolution of the reconstruction is determined with a fully detector simulated Monte Carlo sample corresponding to an integrated luminosity of 1959 (1851) pb^{-1} at $\sqrt{s} = 161$ (172) GeV. Figure 6 shows the selection efficiency, e.g. the ratio of the selected events of all types, to all generated $\mathrm{e^+e^-} \to \gamma\gamma(\gamma)$ Monte Carlo events. For $\cos\theta^* < 0.9$ the efficiency is rather constant, but drops drastically at smaller angles. There are two reasons for this efficiency drop. For acollinear events the angle θ of one cluster may be smaller than the event angle θ^*. If $|\cos\theta| > 0.97$ for at least one cluster this event is not in the acceptance of the selection even if $\cos\theta^* < 0.97$. The cut on the cluster angle θ therefore reduces the efficiency for much smaller $\cos\theta^*$. Furthermore there is more material in the detector at small angles, so more photons convert before the CV and also the number of events with two photons converting is increased. Such events are rejected although the neutral event selection does retain high efficiency for more centrally produced conversions within the drift chambers. The overall efficiency for $\cos\theta^* < 0.9$ is 91.9% with a maximum of 95%. A parametrisation $\mathcal{E}(\cos\theta^*)$ is used for the correction.

The correlation between generated and reconstructed angles is shown in Figure 7A. The Monte Carlo angle is calculated using the two photons with the highest generated energy. Migration occurs only into neighbouring bins. The correlation is very good; incorrectly reconstructed

Process Generator		Number of events expected for 10.3 pb^{-1}
$e^+e^- \to e^+e^-$ (BHWIDE)	[11]	< 0.1
$e^+e^- \to e^+e^-$ (TEEGG)	[12]	< 0.08
$e^+e^- \to \bar{\nu}\nu\gamma\gamma$	[13]	< 0.01
$e^+e^- \to e^+e^-e^+e^-$	[14]	< 0.2
$e^+e^- \to \tau^+\tau^-$	[15]	< 0.003
$e^+e^- \to \bar{q}q$ (PYTHIA)	[16]	< 0.02

Table 3: Estimated contributions from expected background processes. From Monte Carlo at $\sqrt{s} = 161$ GeV.

events would show up as off-diagonal entries. The angular resolution is found to be 0.3° full width half maximum as can be seen in Fig. 7B. An explicit correction for angular resolution is not necessary.

Background is studied using Monte Carlo events from the processes shown in Table 3. No event is selected from any of the samples. Background from cosmic rays is determined to be negligible. In the *I* class a cosmic ray particle must pass the detector near the interaction region in order to fulfil the acollinearity condition. Such a particle passes through the central tracking detectors CV and CJ and is then rejected with the 'neutral event' selection. In the *II* class the cut on $\Delta\phi$ ensures small missing transverse momentum. This means that a cosmic ray particle must cross close to the beam-pipe. Only in the extreme forward and backward region is this possible without passing through CV or CJ. In this case, the event is rejected either by the 'neutral event' selection or the energy condition. For the *III* class the cut on $\sum E$ and p_t will reduce cosmic events, though not suppress them completely. No cosmic event is found within the selected sample by a visual scan. Furthermore the cluster extent is checked as in Ref. [1] since cosmic ray particles normally produce very extended clusters. None of the selected events has a cluster extent in θ or ϕ greater than 0.3 rad that might be an indication of a cosmic ray particle.

The probability that a good photonic event would have been rejected by the neutral event selection due to random hits or instrumental background is studied with random-triggered events. The veto probability for the single veto is $4 \cdot 10^{-4}$ and $1 \cdot 10^{-4}$ for the double veto and the track veto. No correction for the overall veto probability of $5 \cdot 10^{-4}$ is applied since it is small. The systematic errors on the total cross-section are summarized in Table 4.

	Error
Luminosity	0.5%
Radiative correction $\mathcal{R}$	1.0%
Selection efficiency $\mathcal{E}$	1.0%
Background	< 0.3%
Veto probability	0.05%
Sum	1.6%

Table 4: Summary of systematic errors on the total cross-section

6 Results

The fit to the angular distribution is performed using the binned log likelihood method. The likelihood function $\mathcal{L}$ is based on Poisson statistics and defined as:

$$\mathcal{L}_i = \frac{\mu_i^{n_i}}{n_i!} e^{-\mu_i} \tag{15}$$

with n_i the number of observed and μ_i the number of expected events per bin. To determine μ_i the cross-section function $\frac{d\sigma}{d\Omega}$ is not integrated over the bin $[x_l, x_h]$ during the fit. A simple procedure is applied in which the central value x_i of the bin is determined as defined in Ref. [17]. In this way the differential function $\frac{d\sigma}{d\Omega}$ can be directly compared to the integrated number of events presented as a histogram. The mean efficiency $\mathcal{E}_i$ and radiative corrections $\mathcal{R}_i$ are included in the expectation μ_i for each bin. The normalization factor ϵ is added in order to account for the systematic error δ on the total cross-section:

$$\mu_i = \epsilon \, \frac{d\sigma}{d\Omega}(x_i) \; (x_h - x_l)\mathcal{E}_i \mathcal{R}_i L \tag{16}$$

$$\mathcal{E}_i = \frac{1}{n_i} \sum_{j=1}^{n_i} \mathcal{E}(\cos\theta_j), \tag{17}$$

where L is the integrated luminosity, $\cos\theta_j$ is the angle of the j-th event and x_i is determined by:

$$\left(\frac{d\sigma}{d\Omega}\right)_{\text{Born}} (x_i) = \frac{1}{x_h - x_l} \int_{x_l}^{x_h} \left(\frac{d\sigma}{d\Omega}\right)_{\text{Born}} (y) dy. \tag{18}$$

Following the notation in Ref. [19] a χ^2 function is defined. A Gaussian with mean 1 and spread $\delta = 0.016$ (see Table 4) is added to account for the normalization factor ϵ. The routine MINOS [18], which provides accurate asymmetric errors, is used to minimize the χ^2.

$$\begin{aligned} \chi^2 &= \frac{(\epsilon - 1)^2}{\delta^2} + \sum_i -2 \, \ln \mathcal{L}_i \\ &= \frac{(\epsilon - 1)^2}{\delta^2} + \sum_i 2 \, (\mu_i - \; n_i \ln \mu_i) \end{aligned} \tag{19}$$

The fit is performed with two free parameters: The normalization ϵ and the model dependent parameter λ (see Table 5 and eqs. 3, 5 and 8). To obtain the limits at the 95% confidence level the probability is normalized to the physically allowed region, i.e. $\lambda_+ > 0$ and $\lambda_- < 0$ as described in Ref. [19].

The measured differential cross-sections at 161 and 172 GeV centre-of-mass energies are shown in Figure 8 together with a fit of the function $\left(\frac{d\sigma}{d\Omega}\right)_{\Lambda_\pm}$. Results for the different parameters are obtained from the angular distributions for $\sqrt{s} = 161$ and 172 GeV separately and from a simultaneous fit to both distributions. The results are summarized in Table 5. To determine the limit on the mass of an excited electron a fit is performed using $\left(\frac{d\sigma}{d\Omega}\right)_{\mathrm{e}^*}$ (eq. 8). The coupling constant κ for the (e*eγ)-vertex is fixed at $\kappa = 1$. The angular distributions agree well with the QED expectation. The lower limits obtained on $\Lambda_\pm$, Λ and M_{e^*} are higher than existing published results. Previous limits on the excited electron mass with $\kappa = 1$ are $M_{\mathrm{e}^*} > 129$ GeV [35], 136 GeV [34] and 147 GeV [1].

The number of observed events for all classes and the derived total cross-section σ in the range $\cos\theta^* < 0.9$ are compared to the QED expectation in Table 7. The all numbers agree well with QED.

Model	λ	$\sqrt{s}$ [GeV]	Fit result λ	Lower Limits 95% CL Λ_+ [GeV]	Λ_- [GeV]
$\left(\frac{d\sigma}{d\Omega}\right)_{\Lambda_\pm}$	$\pm 1/\Lambda_\pm^4$	161	$\left(0.10^{+5.03}_{-4.63}\right) \cdot 10^{-10}$ GeV^{-4}	174	188
		172	$\left(0.91^{+4.17}_{-3.81}\right) \cdot 10^{-10}$ GeV^{-4}	182	198
		161+172	$\left(0.96^{+3.21}_{-3.01}\right) \cdot 10^{-10}$ GeV^{-4}	194	211
				Λ [GeV]	
$\left(\frac{d\sigma}{d\Omega}\right)_{\mathrm{QED}+7}$	$\lvert 1/\Lambda^6 \rvert$	161	$\left(15.2^{+61.4}_{-91.9}\right) \cdot 10^{-18}$ GeV^{-6}	438	
		172	$\left(7.3^{+44.3}_{-59.0}\right) \cdot 10^{-18}$ GeV^{-6}	466	
		161+172	$\left(10.0^{+35.9}_{-55.8}\right) \cdot 10^{-18}$ GeV^{-6}	479	
				M_{e^*} [GeV]	
$\left(\frac{d\sigma}{d\Omega}\right)_{\mathrm{e}^*}$	$\lvert 1/M_{\mathrm{e}^*}^2 \rvert$	161	$\left(10.7^{+14.1}_{-35.6}\right) \cdot 10^{-6}$ GeV^{-2}	172	
		172	$\left(8.9^{+13.0}_{-30.9}\right) \cdot 10^{-6}$ GeV^{-2}	182	
		161+172	$\left(9.6^{+10.5}_{-29.7}\right) \cdot 10^{-6}$ GeV^{-2}	192	

Table 5: Results for fit parameters λ.

Experiment	$\sqrt{s}$ [GeV]	Λ_+ [GeV]	Λ_- [GeV]
PLUTO [20]	12 – 47	46	36
JADE [21]	12 – 47	66	75
MARKJ [22]	12 – 47	72	–
TASSO [23]	12 – 47	61	56
CELLO [24]	12 – 47	84	44
HRS [25]	29	59	59
MAC [26]	29	66	67
AMY [27]	50 – 66	90	92
VENUS [28]	50 – 66	81	82
TOPAZ [29]	50 – 66	168	97
ALEPH [30]	91	120	129
DELPHI [31]	91	143	120
L3 [32]	91	134	131
OPAL [33]	91	117	110
ALEPH [34]	130 – 136	169	132
L3 [35]	130 – 136	131	167
OPAL [1]	130 – 136	152	142

Table 6: Previous results on cut-off parameters

Energy $\sqrt{s}$ [GeV]	161		172	
	Expected	Observed	Expected	Observed
Number of events				
Class *I*	90.0±0.7	91±9.5	80.1±0.7	78±8.8
Class *II*	8.7±0.2	8±2.8	8.3±0.2	14±3.7
Class *III*	2.2±0.1	3±1.7	1.9±0.1	2±1.4
Total σ [pb]	10.7	10.8±1.1	9.4	9.8±1.1

Table 7: Comparison of number of observed events and Monte Carlo prediction. The derived total cross-section σ and the theoretical value $\sigma_{\mathrm{QED}} = \mathcal{R} \int_0^{0.9} \frac{d\sigma}{d\cos\theta} d\cos\theta$ are given also.

7 Conclusions

The QED process $e^+e^- \rightarrow \gamma\gamma(\gamma)$ has been studied using data taken with the OPAL detector at LEP. The data sample corresponds to an integrated luminosity of 10.3 pb^{-1} at $\sqrt{s} = 161$ GeV and 10.4 pb^{-1} at $\sqrt{s} = 172$ GeV. Both the angular distribution and the total cross-section agree well with QED predictions. Limits are set on cut-off parameters, mass scales for contact interactions ($\gamma\gamma e^+e^-$) and non-standard γe^+e^- couplings, as well as on the mass of an excited electron coupling to eγ with the coupling constant κ fixed at $\kappa = 1$. These limits , summarized in Table 8 are higher than those achieved in previous LEP analyses or by other experiments at lower energies. In the invariant mass spectrum of three final state photons no enhancement for a resonance X decaying like X$\rightarrow \gamma\gamma$ is found. No photonic event with four or five detected photons is observed.

Parameter	Λ_+	Λ_-	Λ_6	Λ_7	Λ_8	M_{e^*}
[GeV]	194	211	789	479	15.4	192

Table 8: Summary of 95% CL lower limits obtained from the combined fit to the $\sqrt{s} = 161$ and $\sqrt{s} = 172$ GeV angular distributions. The results are for the cut-off parameters $\Lambda_\pm$ and mass scales Λ according to QED+6, QED+7 and QED+8 expectation (eqs. 4 – 6). Λ_6 and Λ_8 are derived from Λ_+ and Λ_7 respectively. A lower limit for the mass of an excited electron is also determined.

References

[1] OPAL Collaboration, G. Alexander et al., Phys. Lett. B377 (1996) 222

[2] OPAL Collaboration, K. Ackerstaff et al., CERN–PPE–96–154 (1996), to be published in Phys. Lett.
OPAL Collaboration, Physics Note PN272

[3] F.M. Renard, Phys. Lett. B116 (1982) 269
M. Baillargeon et al., Z. Phys. C71 (1996) 431

[4] F. de Campos et al., HEP-PH/9607241 (1996)

[5] OPAL Collaboration, K. Ahmet et al., Nucl. Instr. and Meth. A305 (1991) 275

[6] F.A. Berends and R. Gastmans, Nucl. Phys. B61 (1973) 414

[7] S.D. Drell, Ann. Phys. 4 (1958) 75

[8] O.J.P. Éboli, A.A. Natale and S.F. Novaes, Phys. Lett. B271 (1991) 274

[9] A. Litke, Ph.D.Thesis, Harvard University, unpublished (1970)

[10] F.A. Berends and R. Kleiss, Nucl. Phys. B186 (1981) 22

[11] S. Jadach et al., University of Tennessee preprint, UTHEP 95-1001 (unpublished)

[12] D. Karlen, Nucl. Phys. B289 (1987) 23

[13] G. Montagna et al., Nucl. Phys. B452 (1996) 161

[14] J. Smith, J.A.M. Vermaseren and G. Grammer, Phys. Rev. D15 (1977) 3280

[15] S. Jadach et al., Comp. Phys. Comm. 66 (1991) 276

[16] T. Sjöstrand and M. Bengtsson, Comp. Phys. Comm. 43 (1987) 367
T. Sjöstrand, Comp. Phys. Comm. 39 (1986) 347

[17] G.D. Lafferty and T.R. Wyatt, Nucl. Instrum. Meth. A355 (1995) 541

[18] MINUIT Reference Manual, F. James and M. Roos, CERN Program Library D506

[19] Review of Particle Physics, R.M. Barnett et al., Phys. Rev. D54 (1996)

[20] PLUTO Collaboration, C. Berger et al., Phys. Lett. B59 (1980) 87

[21] JADE Collaboration, W. Bartel et al., Z. Phys. C19 (1983) 197

[22] MARKJ Collaboration, B. Adeva et al., Phys. Rev. Lett. 53 (1984) 134

[23] TASSO Collaboration, M. Althoff et al., Z. Phys. C26 (1984) 337

[24] CELLO Collaboration, H.J. Behrend et al., Phys. Lett B168 (1986) 420

[25] HRS Collaboration, M. Derrick et al., Phys. Rev. D34 (1986) 3286

[26] MAC Collaboration, E. Fernandez et al., Phys Rev. D35 (1987) 1

[27] AMY Collaboration, H.J. Kim, et al., KEK preprint 89-52 (1989)

[28] VENUS Collaboration, K. Abe et al., Z. Phys. C45 (1989) 175

[29] TOPAZ Collaboration, K. Shimozawa et al., Phys. Lett. B284 (1992) 144

[30] ALEPH Collaboration, D. Buskulic et al., Z. Phys. C59 (1993) 215

[31] DELPHI Collaboration, P. Abreu et al., Phys. Lett. B268 (1991) 296

[32] L3 Collaboration, O. Adriani et al., Phys. Lett. B288 (1992) 404

[33] OPAL Collaboration, M.Z. Akrawy et al., Phys. Lett B257 (1991) 531

[34] ALEPH Collaboration, D. Buskulic et al., Phys. Lett. B384 (1996) 333

[35] L3 Collaboration, M. Acciarri et al., Phys. Lett. B384 (1996) 323

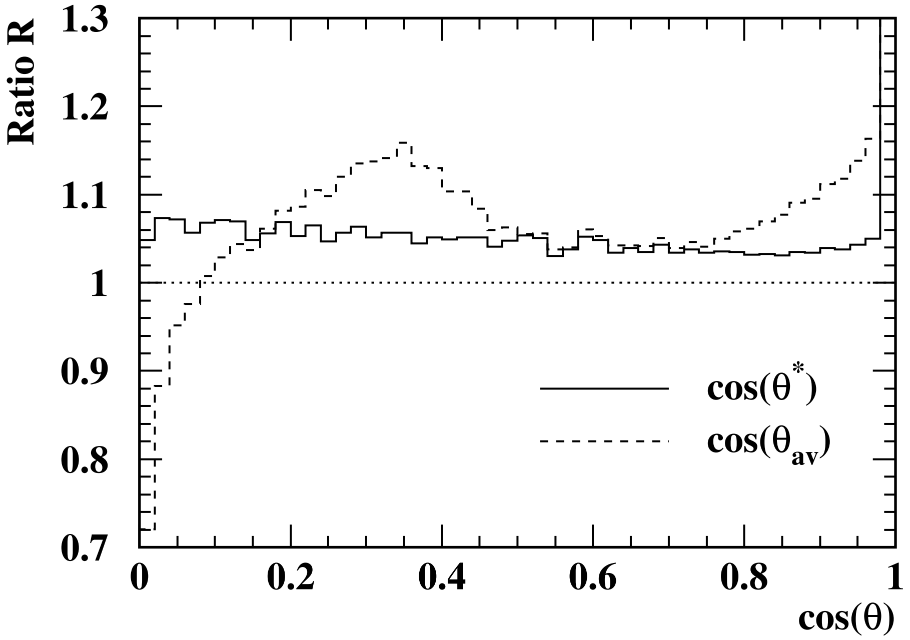

Figure 1: Ratio of the differential cross-section for true Monte Carlo variables relative to the Born cross-section, $\mathcal{R} = \left(\frac{d\sigma}{d\Omega}\right)_{\rm MC} / \left(\frac{d\sigma}{d\Omega}\right)_{\rm Born}$. $\mathcal{R}$ is calculated using the angular definitions $\cos\theta_{\rm av}$ (eq. 8) and $\cos\theta^*$ (eq. 9). The event angle is calculated from the two photons with the highest generated energy.

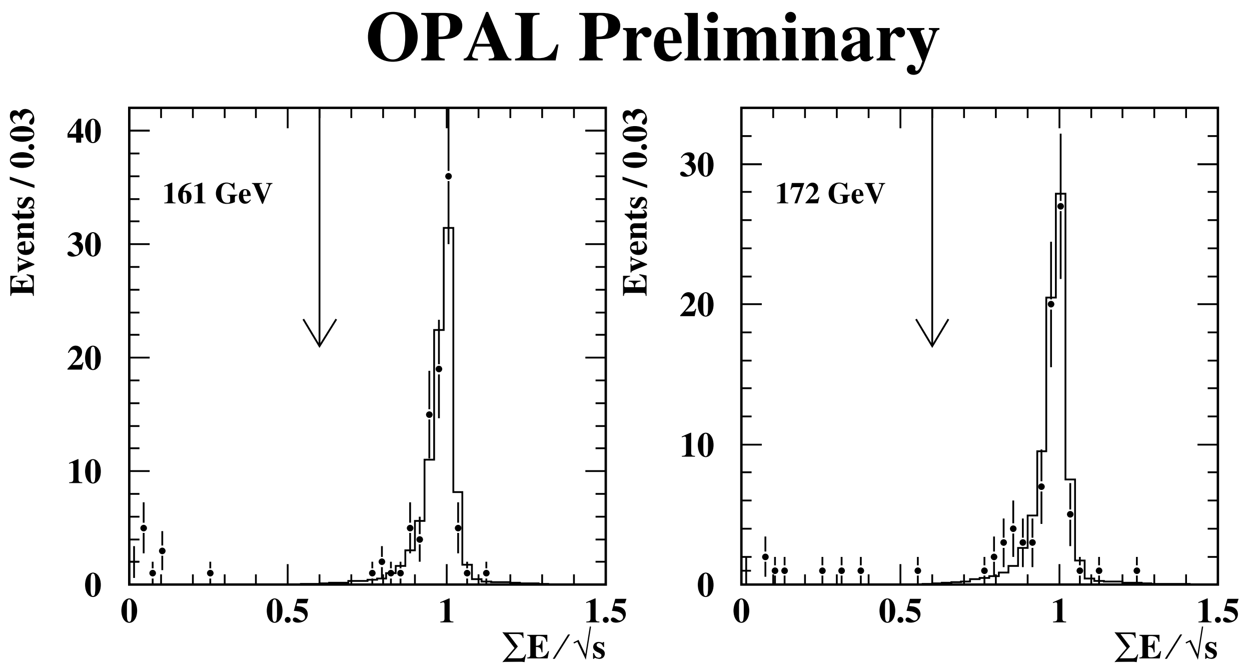

Figure 2: Scaled sum of the cluster energies for events with an acollinearity $\zeta < 10^\circ$ (corresponding to class I). The dots represent data, the histogram $e^+e^- \rightarrow \gamma\gamma(\gamma)$ Monte Carlo expectation. The cut is indicated by an arrow.

OPAL Preliminary

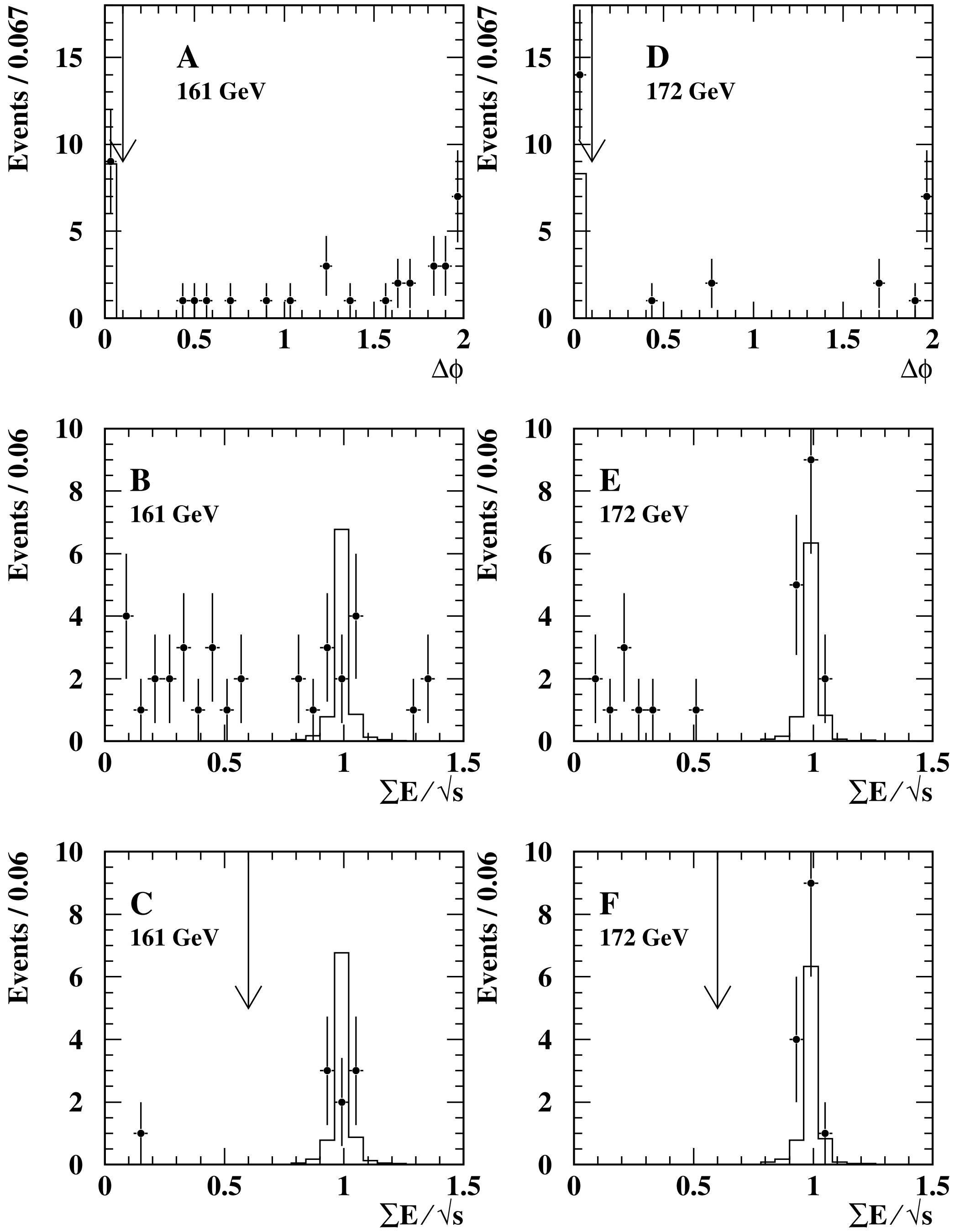

Figure 3: For events of the class *II* plots A and D show the distribution of $\Delta\phi$, a measure of the scaled transverse momentum (definition see text) together with the cut. Plots B and E show the scaled sum of both cluster energies plus E_{gone} and plots C and F show the same distributions after the cut on $\Delta\phi$. Plots A – C are for $\sqrt{s}$ =161 GeV and plots D – F are for $\sqrt{s}$ =172 GeV. The points represent data and the histogram the expectation from $e^+e^- \to \gamma\gamma(\gamma)$ Monte Carlo.

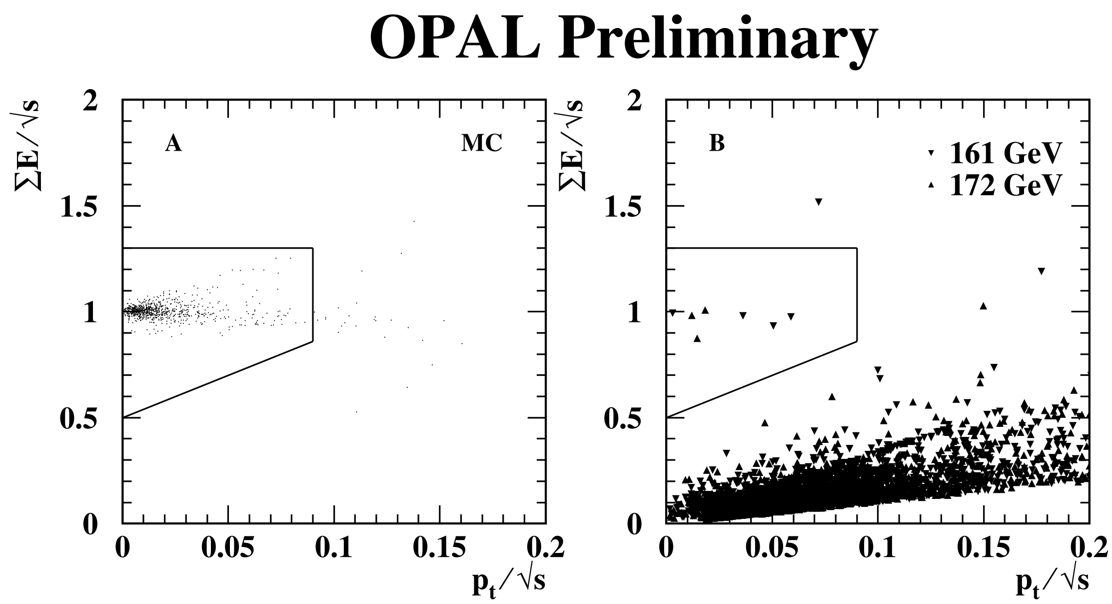

Figure 4: The plot shows the scaled energy sum versus the scaled transverse momentum for the *III* class. Plot A shows $e^+e^- \rightarrow \gamma\gamma(\gamma)$ Monte Carlo and plot B the data for both energies. The curve indicates the cut.

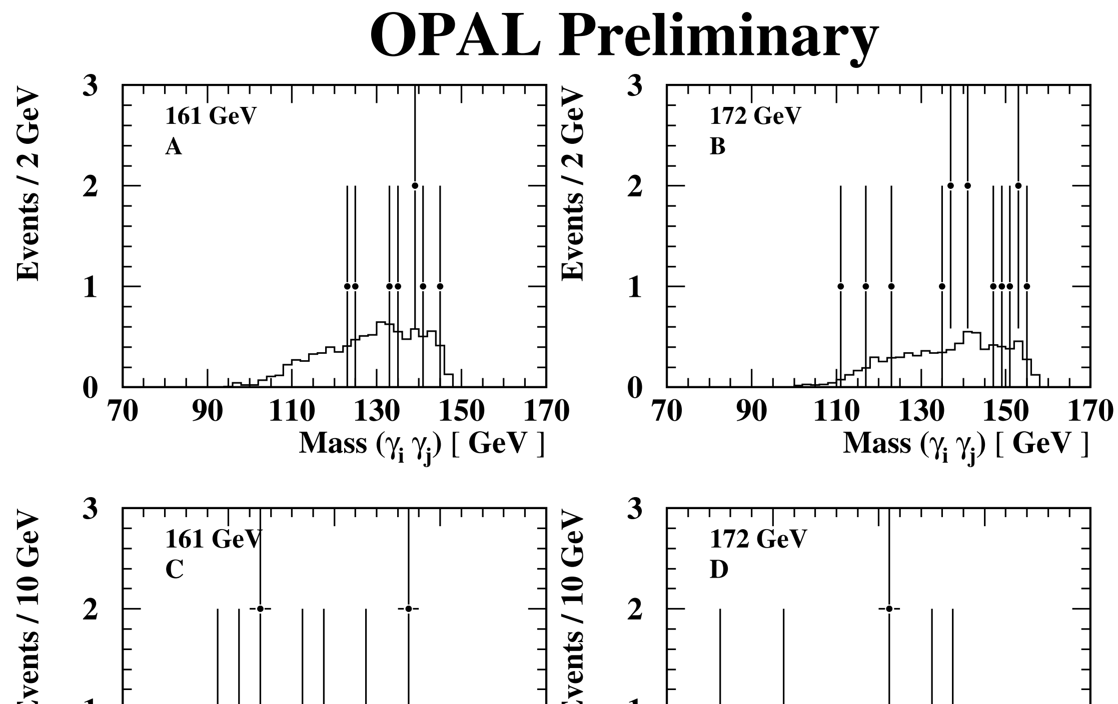

Figure 5: The plot shows the invariant mass of each photon pair for the classes *II* (Fig. A and B) and *III* (Fig. C and D). The points are the data, the histogram the $e^+e^- \rightarrow \gamma\gamma(\gamma)$ Monte Carlo expectation. There is one entry per event in the *II* class and three entries per event for the *III* class.

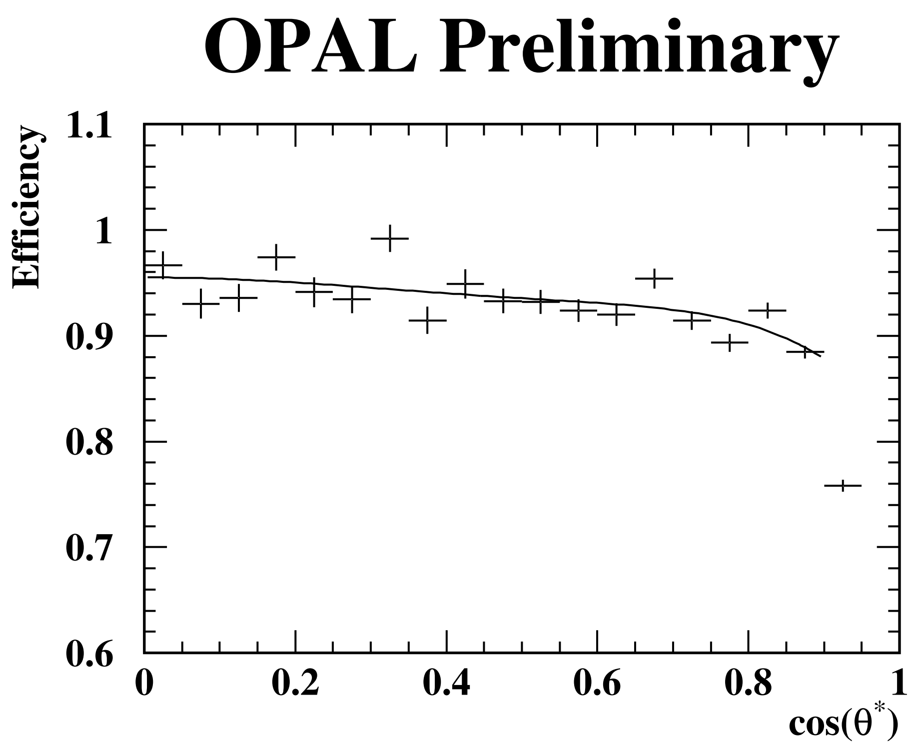

Figure 6: The reconstruction efficiency together with the polynomial fit performed in the range of $\cos\theta^* < 0.9$. The distribution at $\sqrt{s} = 172$ GeV is consistent with the distribution at $\sqrt{s} = 161$ GeV which is shown here.

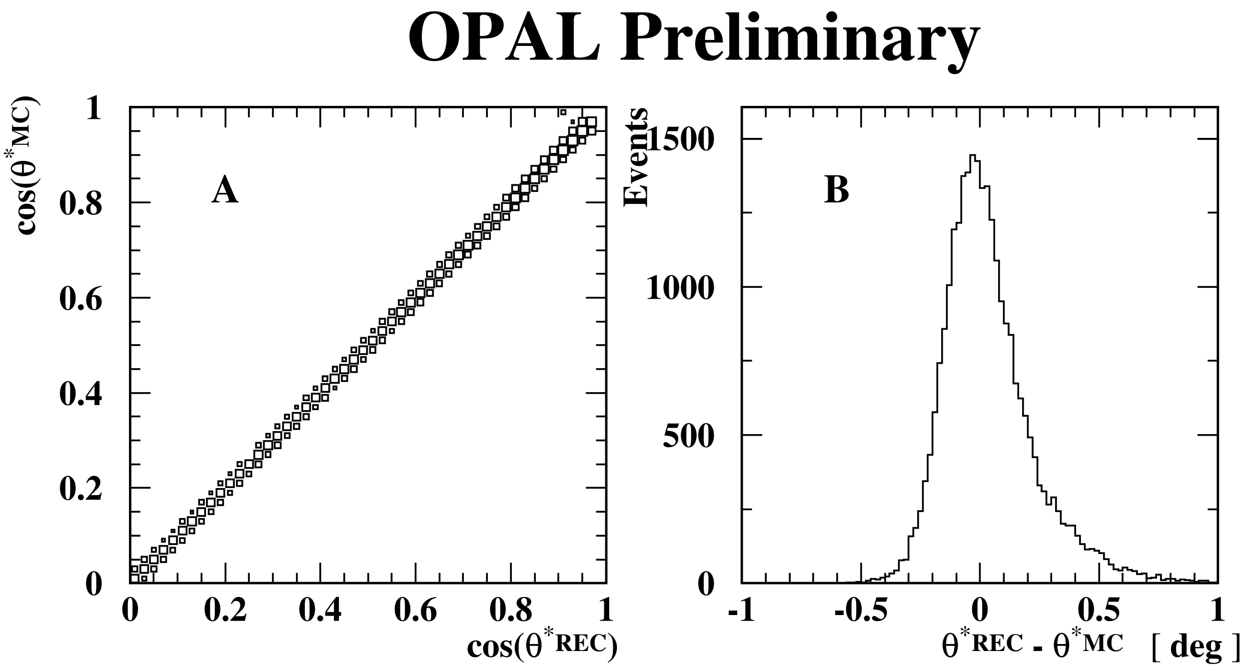

Figure 7: The plot A shows the angular reconstruction, e. g. the correlation between the generated event angle $\theta^*_{\rm MC}$ and the reconstructed event angle $\theta^*_{\rm REC}$ for Monte Carlo events. The size of the boxes is proportional to the logarithm of the number of events. Plot B shows the angular resolution as the difference between the generated and the reconstructed event angle. It is rather independent of the angle θ^*. The distributions at $\sqrt{s} = 172$ GeV are consistent with the distributions at $\sqrt{s} = 161$ GeV which are shown here.

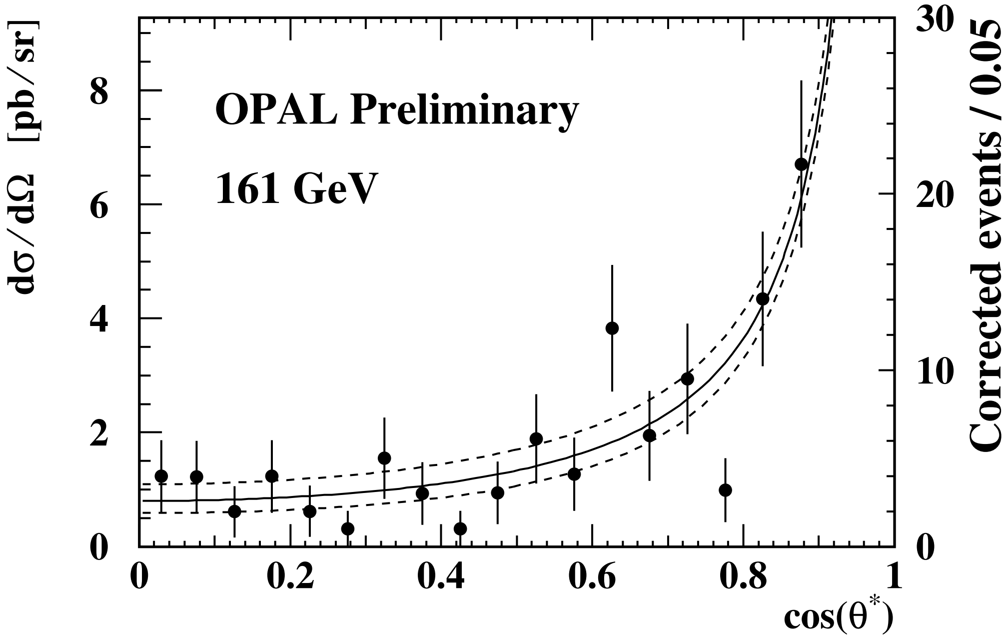

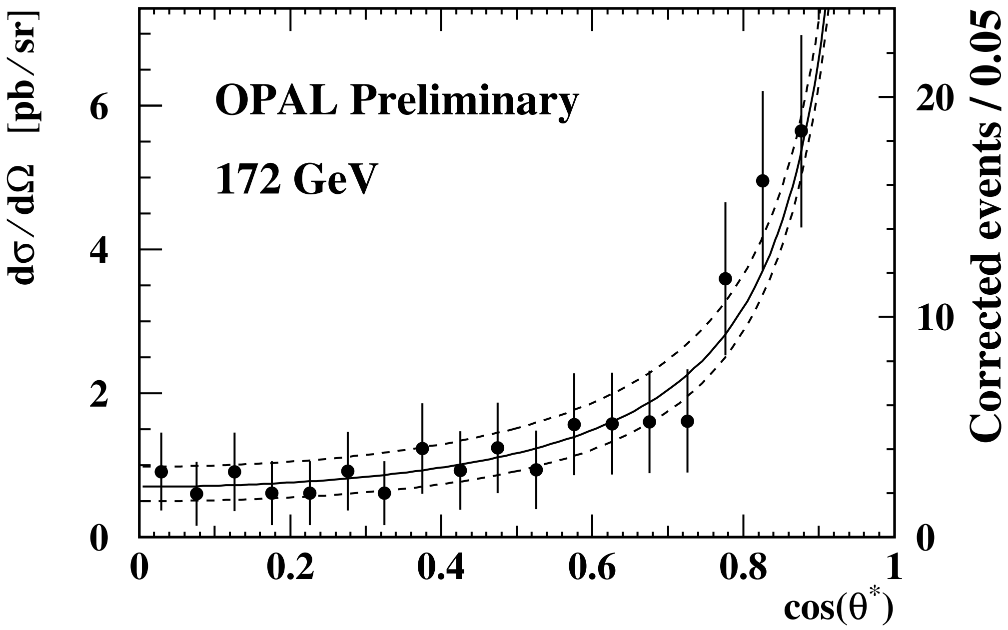

Figure 8: The measured angular distribution of the process $e^+e^- \to \gamma\gamma(\gamma)$ as selected in the three classes. The data points show the efficiency-corrected number of events; radiative corrections are also included. The solid curve corresponds to the Born level QED prediction. The dotted lines represent 95% CL intervals of the fit to the function $\left(\frac{d\sigma}{d\Omega}\right)_{\Lambda_\pm}$.